

Self-Contained Handheld Magnetic Platform for Point of Care Cytometry in Biological Samples

Bekir Yenilmez, Stephanie Knowlton, and Savas Tasoglu*

Magnetic levitation is a powerful tool capable of distinguishing micrometer-scale particles based on their densities. When a particle is suspended in a paramagnetic medium and placed in a magnetic field formed by two permanent magnets with like poles facing each other, the particle will experience two forces—a magnetic force and a buoyant force. These forces cause a particle, such as a cell, which does not necessarily have magnetic properties, to levitate at a height inversely proportional to its density. Magnetic levitation has been shown to be useful for a range of applications, including disease diagnostics, material characterization, and quality control. Here, a portable, self-contained device fully independent from a dedicated microscope or smartphone is developed to levitate particles of interest, image them using an embedded low-cost optical system and a camera module, and process the captured images in order to estimate the densities of the particles. The device is user-friendly and inexpensive, offering a great potential for rapid, on-site sample analysis such as white blood cell cytometry.

1. Introduction

Cell sorting and cytometry, or quantification of the number of cells of interest in a biological sample, is an essential biomedical tool used both in the laboratory and by clinicians as a medical diagnostic test. Several approaches for cell sorting have been proposed to separate cells based on various properties, such as fluorescence-activated cell sorting, which requires fluorescent staining, and magnetic-activated cell sorting, which involves attaching magnetic beads to surface markers. Label-free approaches include dielectrophoresis,^[1] which separates cells based on their dielectric properties and size and Raman-activated cell sorting, which sorts cells based on their intrinsic biochemical profiles.^[2] Microfluidic-based techniques, such as inertial focusing, separate cells based on lift forces,^[3] acoustic-based cell sorting differentiates cells based on a combination of size, density, and compressibility, and optical separation separates cells

based on their refractive index and size.^[4] Label-free approaches eliminate the need for cell markers and allow separation based on intrinsic cell properties.

Magnetic levitation enables label-free, sensitive, and specific density measurements of particles which are suspended in a paramagnetic medium and placed in a magnetic field.^[5–8] A diamagnetic object or immiscible liquid droplet which is suspended in a paramagnetic medium, such as a gadolinium (Gd) ion solution, and placed in a magnetic field will experience two opposing forces: (i) the buoyancy of the object due to its density relative to the medium and (ii) a magnetic force due to its magnetic susceptibility relative to the suspending medium. At equilibrium between these two forces, the object will levitate at a height which is proportional to its volumetric mass density. Magnetic

levitation has been proposed for a wide range of applications, including self-assembly and arrangement of objects,^[9–12] monitoring of chemical reactions and substrate binding,^[13–17] material characterization,^[17–19] bottom-up tissue engineering,^[10,20] and quality control based on the volumetric mass density of the levitated object.^[21,22] This method allows measurements of the intrinsic cell densities and, compared to other label-free approaches, active sorting using a magnetic field formed by two permanent magnets and does not require peripheral equipment to generate the field, reducing the overall cost.

A small-scale magnetic levitation setup compatible with a microscope has previously been developed to separate different types of cells within a blood sample, estimate the age of red blood cells (RBCs), and identify circulating tumor cells.^[5] More recently, a compact, portable, and inexpensive smartphone-compatible magnetic levitation device was proposed to levitate micro-objects, measure the equilibrium levitation height of the object using a smartphone camera and a magnifying lens, and analyze the height to estimate the density of the micro-object.^[23,24] This device was also presented for sickle cell disease diagnostics based on increased density of RBCs in the presence of sodium metabisulfite.^[25] Here, we develop a self-contained magnetic levitation platform fully independent from a dedicated microscope and a smartphone for density-based micro-particle separation from heterogeneous groups of particles, and an algorithm running on the same platform for on-board image analysis and quantification of the levitation height of the particles in order to estimate particle densities. Using this

Dr. B. Yenilmez, Prof. S. Tasoglu
Department of Mechanical Engineering
University of Connecticut
Storrs, CT 06269, USA
E-mail: savas@enr.uconn.edu
S. Knowlton, Prof. S. Tasoglu
Department of Biomedical Engineering
University of Connecticut
Storrs, CT 06269, USA



DOI: 10.1002/admt.201600144

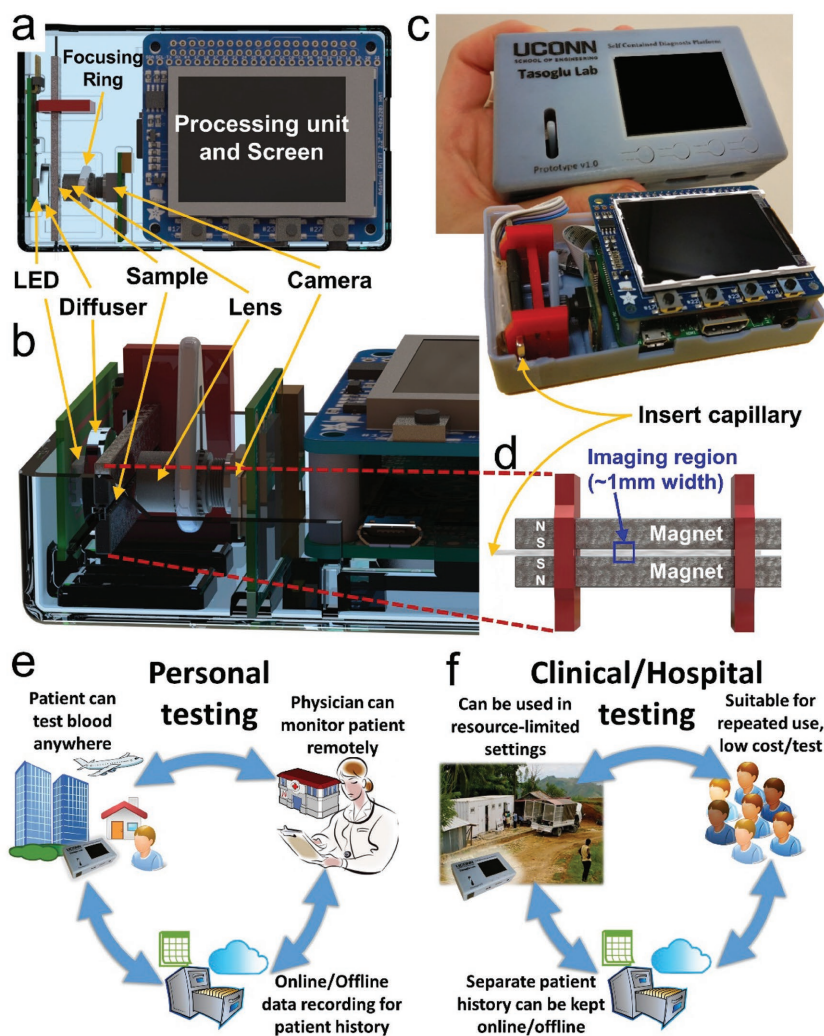


Figure 1. Schematic of self-contained magnetic levitation platform fully independent from a dedicated microscope and a smartphone for density-based microparticle separation. a) Top view of the interior design of self-contained device including the magnetic levitation module, optical components (LED, diffuser, lens, and camera), and the processing unit with screen. b) Close-up view of the magnetic levitation imaging platform. The sample is illuminated by a LED through a diffuser. An image of the sample passes through a lens to the camera, where the image is captured and transferred to the processing unit. c) 3D-printed prototype of the compact and self-contained magnetic levitation and analysis platform. The user inserts a sample of microparticles suspended in paramagnetic solution in a glass microcapillary and controls the device using four buttons on the top face as well as a LED screen displaying the user interface. d) Placement of the magnets and capillary tube for testing. Two permanent NdFeB magnets are fixed in a laser-cut holder 1.1 mm apart with like poles facing each other. The sample, contained in a 1 mm square glass microcapillary tube, is inserted between the magnets to achieve density-dependent magnetic levitation of the microparticles. The sample is imaged in a ≈ 1 mm wide region of the capillary tube, delineated in blue. e) Potential application of the proposed magnetic levitation platform for in-home testing performed by the patient and reported to the physician. f) Potential application of the proposed magnetic levitation platform for use in clinical or hospital settings, including clinics in resource-limited settings.

device, density-based measurements can be carried out without the need for peripheral equipment^[26].

The self-contained platform contains three main components: a magnetic levitation module, optical components, and a processing unit (Figure 1). The magnetic levitation component consists of two magnets fixed in a laser-cut holder and separated

1.1 mm apart such that the like poles are facing each other and the magnetic field is aligned with gravity. A sample is suspended in a paramagnetic medium and loaded into a square glass microcapillary tube via capillary action, then inserted between the magnets (Figure 1d). The magnetic field causes the sample to levitate according to the density of the particles, where denser particles levitate lower than less dense particles. Images of the levitating particles are captured in the area shown in Figure 1d using a custom optical system containing a variable-intensity light-emitting diode (LED), light diffuser, adjustable lens, and camera unit (Figure 1a,b). The images are then processed using the on-board Raspberry Pi, which is a compact, low-cost, single-board computer. This embedded computer runs on a Linux operating system and is loaded with a custom-developed Python code using both OpenCV and custom libraries for image processing and analysis. The embedded system functions to detect the levitation location of the particles in the field of view (FOV) and use this value to estimate the densities of the particles. It can also be used to separate different cell types based on their densities and automatically image and analyze these populations for cytometric analysis of biological samples.

One such cell type of interest is leukocytes, or white blood cells (WBCs). These cells are generally responsible for fighting infections. In the blood, WBC counts higher or lower than the normal range ($3500\text{--}11\,000\ \mu\text{L}^{-1}$) can be a useful diagnostic indicator. High WBC counts may indicate infection, immune system disorders, or leukemia; low WBC counts may indicate an autoimmune disorder or conditions that damage the bone marrow, such as leukemia. Tracking WBC levels is critical in patients undergoing chemotherapy or those with human immunodeficiency virus (HIV).

Clinically, WBC cytometry may be done visually under a microscope by a trained user. Alternatively, density-based separation, or fractionation, of RBCs and WBCs can be performed where the denser RBC fraction is separated from the less dense WBC fraction via centrifugation in a density gradient medium. However, this protocol requires several steps by the user and downstream cell counting to quantify the isolated WBC population. To streamline this common test, medical devices have been developed to perform the analysis; however, these devices generally require reagents or stains to distinguish the cell population of interest. Laboratory devices, such as the Sysmex XE 2100, use flow cytometry to quantify the WBC population. In this assay,

the sample is stained with a fluorescent polymethine dye, which stains nucleic acids and organelles, and treated with a surfactant, which lyses the RBC membranes.^[27] Hence, fluorescence intensity and forward scatter (related to size) allow WBCs to be differentiated from RBCs or nucleated RBCs and quantified. However, this technology is very costly and requires extensive specialized training, making it incompatible with point-of-care (POC) settings such that samples must be sent to centralized testing labs for testing. To address this issue, a portable, on-site device, the Hemocue WBC System, counts WBCs from whole blood loaded into a cuvette where the RBCs are lysed and a stain marks the WBCs. The sample is then optically imaged to count the number of stained cells. While this POC-compatible device has shown promise in making this test available on-site, the list price is over \$600,^[28] making it inaccessible to a large population such as those in developing countries.

In contrast, the process presented here does not require any cell lysis buffer or stains to perform the analysis. This cell-based test takes advantage of the unique inherent densities of the two cell types to perform separation. Only a low-cost paramagnetic solution in a sample tube is needed to perform the test; the cost of these consumables is less than \$1 per test. Further, the device is lower cost than available automated technologies, estimated less than \$100.

Due to the user-friendly sample preparation and user interface, this device can be applied to clinical diagnostic needs either by facilitating in-home patient testing or as a tool for healthcare settings, including limited-resource settings (Figure 1e,f). The patient data can be transferred from the presented self-contained device via Bluetooth (not presented here) or a cable to a computer, a smartphone, or a satellite phone in areas where cellular or radio coverage is either unavailable or inaccessible.

2. Results and Discussion

2.1. Magnetic Field Characterization

The magnetic field components are given in the Supporting Information. Equations (2), (3), and (4) of the Supporting Information were solved to plot the magnetic field distribution (Figure 2b,c). Based on this result, microparticles will be driven toward regions of minimal magnetic flux density (along the centerline between the two magnets) (Figure 2b) and can be spatially confined in 3D or 2D magnetic traps.^[5,10,20,25,29,30] Figure 2 shows the theoretical and experimental behavior of microparticles suspended in a paramagnetic medium and placed in a magnetic field (Figure 2a).^[23] The equilibrium levitation height of a particle depends of two forces: (i) the gravitational buoyant force (F_g) due to the density of the particle relative to that of the suspending medium, and (ii) the magnetic force, which depends on the magnetic susceptibility of the particle (which is very low for diamagnetic particles such as the polystyrene microspheres used here) relative to that of the paramagnetic suspending medium. In the case where a particle is denser than the paramagnetic medium, a downward F_g acts on the particle. Similarly, in the case where the particle is less dense than the paramagnetic medium, an upward F_g acts

on the particle. The magnetic force acting on the particle has a directionality toward the centerline between the two magnets (Figure 2b) with magnitude greatest at the surface of the magnets (0.15 T) and approaching zero at the centerline between the magnets (Figure 2c). The balancing of these forces creates a line of equilibrium (horizontal in the FOV) at which the two forces are opposite and equal to each other where particles of the same density will levitate. In the case where the particles are denser than the medium, the downward F_g will be balanced by an upward F_m of equal magnitude at a point below the centerline. In the case where the particles are less dense than the medium, the upward F_g will be balanced by a downward F_m of equal magnitude at a point above the centerline. When these forces are unbalanced, the particle will move in the field and this motion is opposed by a drag force (F_d) until equilibrium is reached (Figure 2a).

It should also be noted that a magnetic force also acts in the X-direction (the axis along which the image is captured) toward the centerline of the magnets. This causes particles to levitate along a narrow Y–Z focal plane. The optical components are adjusted by the user such that this plane is focused by the lens onto the camera detector, allowing in-focus imaging of the particles once they reach this plane. Images of particles immediately after insertion in the magnetic field will be seen out of focus as they are homogeneously distributed. However, as the particles move toward a single focal plane, individual particles may be resolved.

These forces cause a nonlinear equilibration of the particles over time (Figure 2e–j). The concentration of Gd in the paramagnetic medium directly affects the time to equilibrium (Figure 2e–g). The upper and lower limits of the particles are tracked over time (Figure 2e,f). The equilibrium time is defined as the point at which the distance between the upper and lower limits reaches 20 μm . Higher concentrations of Gd increase the magnitude of the magnetic force and, therefore, both shifts the levitation height at equilibrium toward the centerline (which is consistent with Equation (5), Supporting Information) and decreases the time for a particle to reach equilibrium (which is consistent with Equation (7), Supporting Information) (Figure 2g). Testing of a range of different size microspheres demonstrates that the equilibrium levitation height of the particles is independent of particle size (Figure 2h–j); this result agrees with the analytical model (Equation (5), Supporting Information). However, the time to equilibrium is inversely related to the microsphere size, which is also consistent with the analytical model (Equation (7), Supporting Information).^[5,30]

In order to predict any negative effect of the magnetic field on the electrical components, the magnetic field at the camera board, which is the closest component susceptible to the magnetic field, was modeled mathematically (Figure 2d). The greatest magnitude is ≈ 1.4 mT. Further, no malfunction of electronic components has been observed through the duration of these experiments.

2.2. Image Quality Characterization

The uniformity of illumination was quantified across the FOV (Figure 3a). Pixel intensity and variation are measured as a

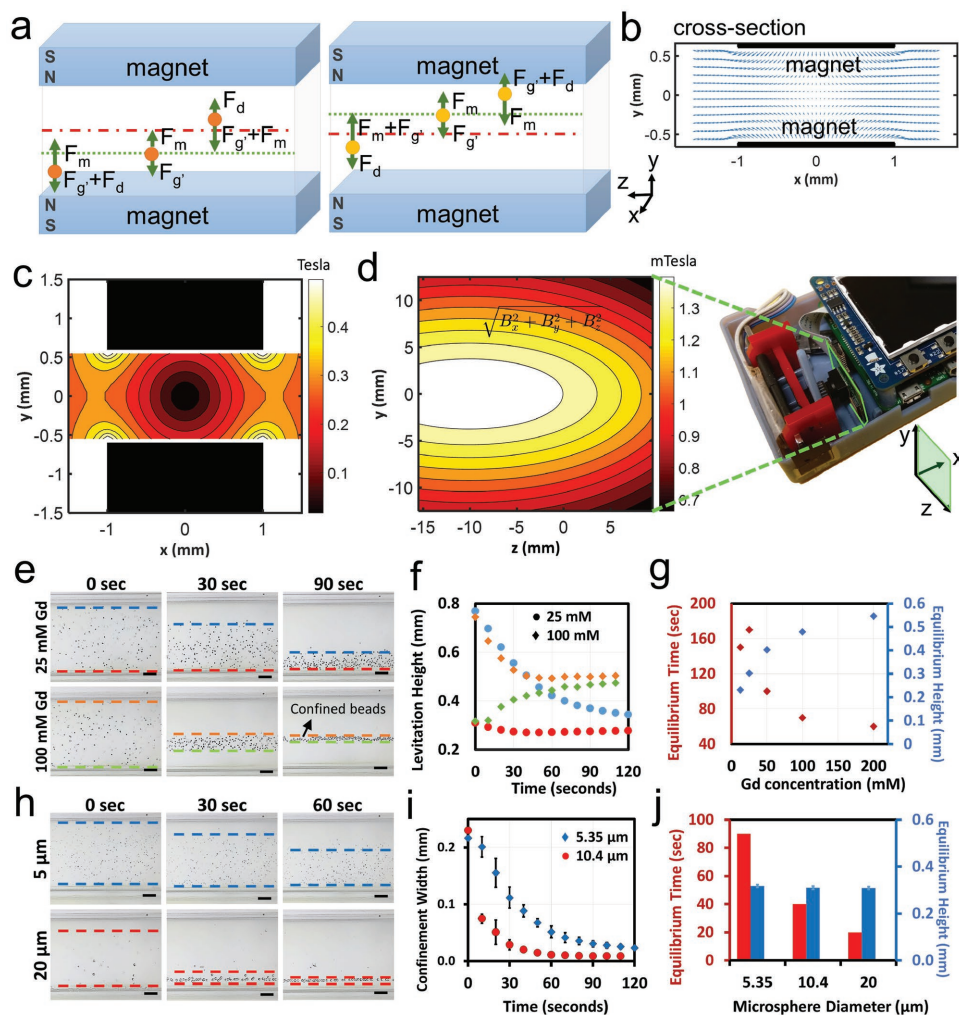


Figure 2. Characterization of the self-contained magnetic levitation platform. a) Magnetic levitation of a particle which is more dense (left) and less dense (right) than the paramagnetic medium. The particle experiences (i) a gravitational buoyant force (F_g), which is downward in the case of a more dense particle and upward in the case of a less dense particle relative to the medium, and (ii) a magnetic force (F_m) acting in the direction toward the centerline. Therefore, the particle will move toward an equilibrium levitation height (below the centerline in the case of a denser particle, left, and above the centerline in the case of a less dense particle, right), at which these forces are equal and opposite. A drag force, F_d , also acts on the particle as it moves toward the medium until it reaches equilibrium. b) Cross-section of the plane passing through the center of the magnets showing the directionality of the magnetic field toward the centerline between the magnets. The reference of all the axes in the figure is at the centroid of the magnets. c) Contour plot of magnetic field at the cross-section of the plane passing through the magnets. The force is greatest at the surface of the magnets and approaches zero at the centerline between them. d) Total magnitude of the magnetic field on the camera board. e) Representative images demonstrating the effect of Gd concentration on levitation height and time to equilibrium for $10\ \mu\text{m}$ particles. f) Upper and lower limits of the particle levitation over time for two different Gd concentrations. g) Quantification of the effect of Gd concentration on equilibrium time (red) and levitation height at equilibrium (blue). h) Representative images demonstrating the effect of particle size on levitation height and time to equilibrium in $50 \times 10^{-3}\ \text{M}$ Gd. i) Upper and lower limits of the particle levitation over time for two different particle sizes. Data points are the average over five trials with error bars representing the standard deviation. j) Quantification of the effect of particle size on equilibrium time (red) and levitation height at equilibrium (blue).

function of the Z-position (as illustrated in Figure 3d). The average intensity represents the mean pixel intensity in vertical slices, showing that the brightness is approximately equal between the left and the right of the FOV (within 5%). Further, the variation represents the standard deviation in pixel intensities within vertical slices, demonstrating low variance from top to bottom between the magnets ($\pm 15\%$).

The distortion of the captured image is also quantified across the FOV from left to right (Figure 3b). As the image is distorted by compression at the edges of the FOV, the distance between

the straight edges of the two magnets is plotted across the Z-axis (defined in Figure 3d) as a percent decrease relative to the same measurement at the center of the FOV. The distortion is below 3% across the entire FOV.

Bead sharpness was also quantified as the maximum pixel-to-pixel change in intensity along a profile line radiating from the center of the microsphere (Figure 3c). The bead sharpness was plotted as a function of the horizontal distance of the bead from the center (as defined in Figure 3d). The average bead sharpness is within one standard deviation in the center 75% of

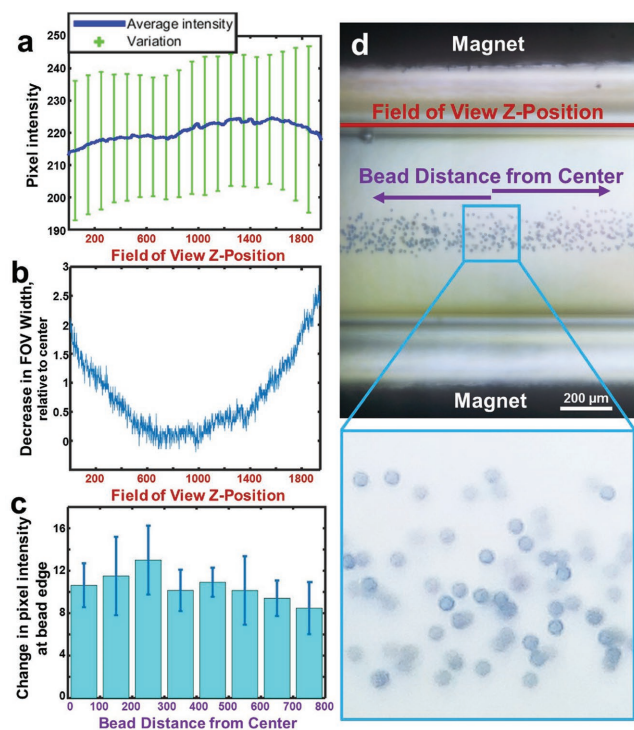


Figure 3. Characterization of image quality. a) Uniformity of illumination within the FOV. Average intensity represents the average brightness, or pixel intensity, within 1-pixel wide vertical slices across the FOV in the area between the magnets (with no sample present). The variation represents the standard deviation of pixel intensities in 100-pixel wide vertical bins between the two magnets. b) Distortion in the FOV, as measured by the vertical distance between the two straight magnet edges. All measurements are expressed as a percentage decrease in distance between the magnets relative to the average measurement in a 100-pixel slice about the center of the FOV. c) Bead sharpness as a function of the horizontal distance of the bead from the center of the FOV. Sharpness is defined as the greatest pixel-to-pixel change in intensity along a profile drawn from the center of a microsphere to a point outside the microsphere. d) Representative image of the imaging FOV, showing the magnetic levitation of 10 μm microspheres.

the FOV, with only a slight decrease in sharpness at the edge of the FOV. Microspheres could be resolved across the entire FOV.

These results indicate that the platform presented here offers a greater uniformity of illumination and particle sharpness and experiences less distortion at the edge of the FOV compared to the smartphone-compatible device presented previously.^[23,25] While the smartphone camera used in the previous setup (the Samsung Galaxy S4^[23,25] did have a higher resolution (13 Megapixels compared to the 5 Megapixels used here), the images in the smartphone-compatible setup are not limited by resolution but rather are limited by the range of focal distances possible in the built-in camera. The lens in this device could be separated from the camera board at an ideal position to achieve optimal magnification and imaging quality. Further, most smartphones available on the market do not offer manual focusing capabilities; images are limited by the software's autofocus capabilities (with few exceptions in high-cost smartphones). In contrast, this device includes a focusing lever with which the user may manually adjust the position of the lens to obtain the optimal

focus. Increased image quality offered by this device compared to smartphone-compatible devices may ultimately improve the ability to image small particles and, therefore, maximize the sensitivity and accuracy of medical diagnostics.

2.3. User Interface

The thin-film transistor (TFT) display screen and four buttons serve as a user interface to control image capturing from the main screen (Figure 4a). When the user inputs a sample into the device, fine focus is achieved by pressing button 1 (far left

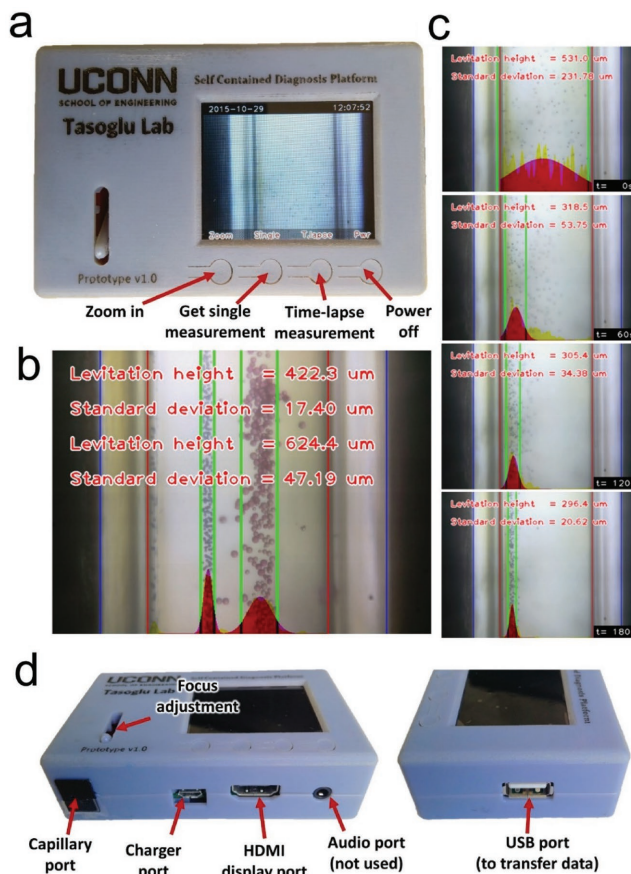


Figure 4. User interface and data output. a) The user interface allows the user to view the levitating particles (magnets are seen on the left and right, where the magnet on the left side of the image is the bottom magnet). From the main menu, the user can also zoom in on the image to focus the setup, capture a single image, capture time lapse images at 10 s intervals, or power the device on/off using the buttons located below the screen. b) Captured image at equilibrium of a mixture of two microspheres with different densities. The processing algorithm is able to determine the levitation height relative to the bottom magnet and the standard deviation of the particles for one or more populations of microspheres. All measurements are scaled from pixels to micrometers using the ratio between the known inner diameter of the microcapillary, 0.7 μm , and the measured distance. c) Demonstration of the time lapse imaging and analysis feature. Images are captured every 10 s over a number of minutes selected by the user (here, images were taken over 3 min). d) Ports and features for user interface, including a capillary port for inserting the sample, a focus adjustment lever for fine focus of the sample, and charging and data ports.

button) to zoom in (5× digital magnification) and moving the fine focusing lever to find the optimal focus setting. Button 2 captures a single image of the sample and processes it to determine the levitation height and standard deviation (Figure 4b). Button 3 begins capturing an image every 10 s for a total time set by the user and processes the sequence of images (Figure 4c). By default, six images are captured; buttons 1 and 2 can be used to increment or decrement this value by an interval of six images (respectively). The images are also stored onto a USB flash drive for later use (Figure 4d). The ensuing image processing, as described in the following section, then extracts information about the sample by analyzing the series of captured images, outputting relevant information pertaining to the densities of the particles in the sample. The far right button (button 4) functions as a power button.

2.4. Image Analysis Algorithm

Three main feature detection functions are performed within the device to assess the levitation of the particles within a captured image (Figure 4b,c). A Gaussian curve is generated from pixel intensity gradients across the FOV and the mean of this curve is considered the average levitation height of the particles. The magnet edge is used as a frame of reference, with the levitation height expressed as the distance from the bottom magnet edge. The standard deviation of the Gaussian curve is also reported as a measure of the variation in the particles,

which represents the width of confinement. The capillary edges are used to calibrate the scale of the image by calculating the pixel distance between the two edges; since this distance is known to be 0.7 mm, the ratio between these distances is used to convert levitation measurements from pixels to millimeters. In Figure 4b, two particles with different densities are used to demonstrate the ability to detect two distinct populations.

2.5. Characterization of Magnetic Levitation

Density-controlled microspheres were used to calibrate particle density to levitation height (Figure 5a,b). The result shows that the levitation height (relative to the bottom magnet) and density of the microspheres are inversely related and the relationship is approximately linear. These linear approximations may be used as calibration curves to estimate the density of any particle from its levitation height given a known Gd concentration. Based on the theoretical model, equilibrium height, h , (given in Equation (5), Supporting Information) is linearly dependent on the density of the particle. Also, the distance between h and the magnet mid-plane is inversely proportional to the concentration of Gd in the suspending medium.^[5] The approximately linear calibration curves obtained experimentally are consistent with the theoretical model.

The greater concentrations of Gd tested allow for measurement of a larger range of microsphere densities. On the other hand, smaller concentrations of Gd offer a greater difference

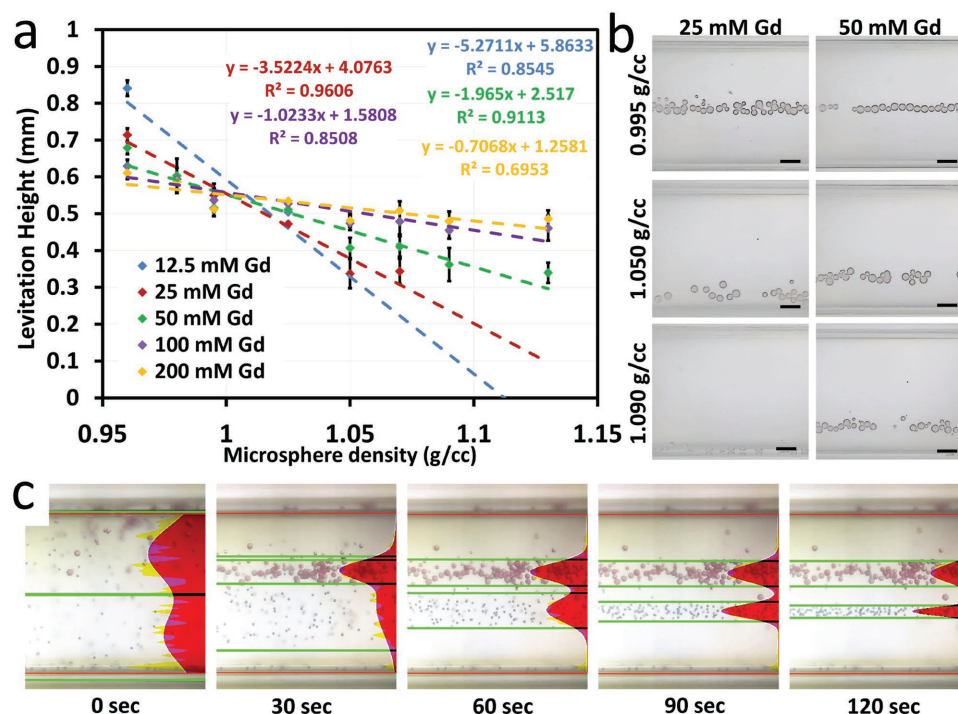


Figure 5. Portable and self-contained magnetic levitation platform for density measurement and separation of microparticles. a) Linear calibration curves correlating microsphere density to levitation height for five different Gd concentrations ranging from 12.5×10^{-3} to 200×10^{-3} M. The correlations are approximately linear ($R^2 > 0.7$). The slope is greatest when the concentration of Gd is the least, indicating a greater degree of sensitivity to small density differences. The slope is lowest for greater concentrations of Gd, demonstrating the increased range of detection. b) Representative images showing the levitation of different density microspheres in varying concentrations of Gd. Images enhanced for visibility. c) Imaging and processing of the levitation of a mixture of two different density microspheres over 2 min, showing distinct bands of confinement of the respective populations at equilibrium.

in levitation height for smaller differences in density; that is, smaller Gd concentrations offer a greater resolution of density detection. However, the high-density beads levitated with low concentrations of Gd were observed to settle to the bottom of the capillary because the magnitude of the buoyant force was significantly greater than the magnetic force under these conditions, indicating that low Gd concentrations result in a limited range of detection. This result is also consistent with the theoretical model given by Equation (5) in the Supporting Information. The experimental error in levitation height in each of the six data points tested was within 0.039 mm at 12.5×10^{-3} M Gd and 0.026 mm at 200×10^{-3} M Gd. This corresponds to an error of 0.007 g cc^{-1} at 12.5×10^{-3} M Gd and 0.037 g cc^{-1} at 200×10^{-3} M Gd.

Figure 5c demonstrates the ability to separate particles of different densities and identify their respective levitation heights and standard deviations using the image processing algorithm.

2.6. Cost Analysis

Table 1 shows the total cost estimate of a single self-contained magnetic levitation platform. The total cost is below \$100, which is lower than other available POC technologies. As the greatest costs are due to the use of commercially available products, the cost may be further reduced by custom designing and mass manufacturing the components for this specific purpose.

Cost considerations are important in the design of POC devices, particularly for low-resource settings. The majority of the cost associated with this device is due to the presence of a processing board, camera, and TFT display (Table 1)— $\approx 75\%$ of the cost of the device. However, this includes the cost associated with the necessary imaging and processing, which is critical for use of magnetic levitation technology in POC settings. With the previously developed smartphone-compatible device,^[23] the imaging and processing is performed by a user-provided smartphone. While the user may already own a smartphone, it is unlikely that, in clinical settings, a clinician would be able to use their personal device considering privacy concerns. Purchasing this device (such as the Samsung Galaxy S4 which was used previously^[23,25]) adds an additional cost which is generally over \$100, exceeding the cost of the self-contained device presented here. Thus, by forgoing the unnecessary yet costly features contained in a smartphone, the device presented

Table 1. Cost estimate per device.

Device component	Estimated cost (per device)	High-volume, 1000 pcs cost (per device)
3D printed casing (raw materials only)	\$5	\$2
Raspberry Pi model A+	\$24.95	\$19.00
Adafruit PiTFT 2.2" TFT	\$24.95	\$19.96
NdFeB magnets (2)	\$6.32	\$3.64
Raspberry Pi camera board	\$19.95	\$14.00
LED illumination	\$5	\$3.00
Total cost	\$86.17	\$61.06

here can be obtained at a lower total cost than a smartphone-compatible device including the smartphone.

2.7. Levitation of WBCs in Blood

Figure 6 shows a useful application of this platform to levitate and isolate WBCs in blood for rapid, automated cytometry. In Figure 6a, the region of levitation for the WBC population can be identified by lysing the RBC population with ACK buffer and levitating the sample (the pictured sample has been concentrated for better visualization). This region defines the region for counting WBCs in subsequent experiments.

Figure 6b demonstrates a method of sampling to count WBCs within the defined levitation area. Similar to the use of a standard hemocytometer, the cells within a set region (i.e., the FOV of one image) are counted; this process is repeated in 10 randomly selected regions throughout the capillary tube by shifting the sample through the magnets slightly, capturing an image at each location. The WBCs, defined as particles within the levitation region set in Figure 6a, may be counted in each image and averaged. The width of the region in the FOV is 1 mm and the cross-sectional area of the capillary is 0.7 mm by 0.7 mm. Thus, the volume of the sample in each FOV is $\approx 0.5 \mu\text{L}$. Multiplying the average number of WBCs per FOV by a factor of 2000 will correct for this volume and the sample dilution (1:1000 in this experiment) to give the number of cells per microliter (where the normal range is generally considered to be 3500–11 000 WBCs μL^{-1}).

Where other technologies use lysis buffers to remove RBCs or stains to identify the WBC population, this approach can perform density-based separation of RBCs and WBCs and isolate the WBC population with no lysis step necessary. Figure 6c shows the effective separation of the RBC and WBC populations in 25×10^{-3} M Gd after 10 min. The RBCs levitate at a lower height (with many along the bottom of the capillary) than the WBCs. This result is consistent with previous literature: the majority of the WBC population has been reported to be less dense than the RBC population (as calculated via density gradient centrifugation^[31]). Further, different types of WBCs have differing densities ranging from 1.060 to 1.110 g cc^{-1} ,^[31] which explains the broad spread of levitation heights observed. A concentration of 25×10^{-3} M Gd was selected for this application in order to achieve the maximum possible separation between the RBC and WBC populations (for more reliable detection) without allowing the WBC population to reach the bottom of the range allowed by the sample tube.

3. Conclusion

Here, we present a portable, self-contained platform composed of a core module utilizing the principles of magnetophoresis for microparticle separation,^[5] and embedded components including an embedded computer, a TFT screen, a camera, and optical components (variable-intensity LED, light diffuser, and adjustable lens with a focus ring). Magnetic levitation and density-based analysis of micrometer-scale particles via the presented platform is label-free and highly sensitive. Compared to

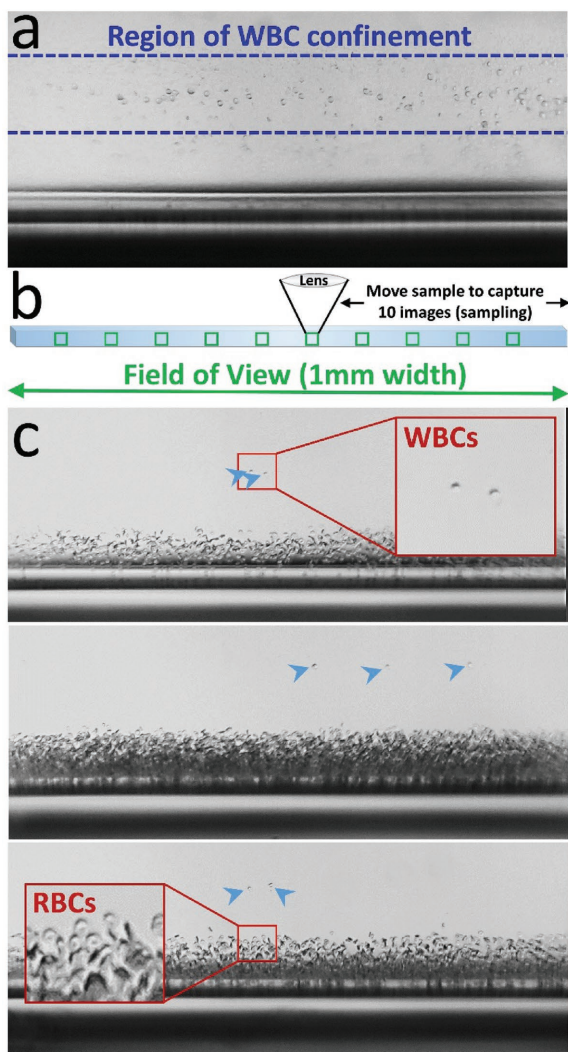


Figure 6. Label-free identification of WBCs in blood. a) Confinement of WBCs, where RBCs have been lysed (25×10^{-3} M Gd, 10 min levitation period). The confinement region of WBCs is outlined in blue. b) Schematic for WBC quantification: the sample is moved through the space between the magnets to capture 10 images randomly spaced throughout the entire sample contained in the capillary tube. Each imaged region is about 1 mm in width and represents a $0.5 \mu\text{L}$ volume. The total concentration of WBCs per microliter in the sample is equal to the average number of WBCs per FOV multiplied by a factor of 2000. c) Separation of WBCs (higher levitating population) from RBCs (the population at the bottom of the capillary). Inlays show WBCs (top) and RBCs (bottom). WBCs are marked with blue arrows to demonstrate the ability to quantify the number of cells in each FOV. Whole blood was diluted 1:1000 in 25×10^{-3} M Gd and imaged after 10 min in the magnetic field.

previous technologies, this device has smaller-scale detection capabilities than other devices presented.^[9,13,21,30,32] Further, the device is more portable and user-friendly than similar microscopy-compatible setups,^[5] and offers fully self-contained image capture and analysis.^[23] Use of on-board optical imaging and analysis allows quantitative analysis of a population of micrometer-scale particles. The device is also low-cost (less than \$100 per device) and is less than \$1 per assay, making the device promising for in-home or low-resource applications. The wide

range of practical applications, including quality control and disease diagnostics, will benefit greatly from the on-site capabilities offered by this device.

Although the smart-phone attachable magnetic levitation device developed previously^[23] and several other smart-phone-attachable devices are similarly portable and inexpensive, potential difficulties in standardization via different smart-phone brands or hardware, operating systems (iOS, Android, Symbian, RIM, etc.), and/or different versions of the same brands may cause an inconvenience for health technicians, doctors, or patients, especially in resource-limited settings. Here, the patient data can be transferred from the presented self-contained device via Bluetooth (not presented here) and/or a cable to a smartphone or computer. Therefore, a variation in the hardware or software of the local user's device will not affect the quality of diagnosis and monitoring of disease, but such internet-connected devices can be used for data transfer and communication if necessary. For example, the proposed self-contained device can be connected to satellite phones in areas where cellular or radio coverage is unavailable or inaccessible.

The presented platform does not require a dedicated microscope for small-scale imaging, antibody labels to distinguish particles, or complex assay protocols for reliable diagnostic testing. In contrast to other automated devices, the simplified process presented here does not require RBC lysis reagents or stains to identify WBCs. Rather, this test leverages the unique inherent densities of WBCs compared to RBCs to perform rapid, label-free separation. For this reason, the cost of the consumables is less than \$1 per test, comprising only a sample tube and a low-cost paramagnetic medium.

These results demonstrate the ability to perform cell cytometry of a particular population of cells (WBCs) from a mixed population in human blood. While additional clinical studies must be performed to validate this application in a large patient population, these results demonstrate promise for WBC cytometry as well as other applications to quantify a particular population of cells in blood or in other body fluids such as urine or saliva. The device may also be used for cell biology research in resource-limited settings or as a teaching tool in schools, as density differences observed using this device can reflect several events such as the cell cycle, phagocytosis, apoptosis, and differentiation.

4. Experimental Section

Device Fabrication: The magnetic levitation device casing was custom designed using CAD software and 3D printed using an Objet30 Prime (Stratasys, Eden Prairie, MN), a high-resolution PolyJet-based 3D printer with a $32 \mu\text{m}$ layer height^[33,34]. Within the casing, a Raspberry Pi embedded computer and TFT display (Adafruit, New York, NY) are stacked and fixed in place. A 5-Megapixel camera module (v1, 1367, Adafruit, New York, NY) is also placed in the device and connected to the board via a ribbon cable. The camera module is modified by taking apart the lens and adding a custom extension tube between the sensor and the lens. This adjustment increased the magnification of the image on the sensor considerably, thus making it unnecessary to use an additional lens which would decrease the image quality and increase the cost. The magnetic levitation module is assembled from two 2 mm by 5 mm by 50 mm NdFeB permanent magnets (K&J Magnetics, Inc., Pipersville, PA), which are magnetized through the 5 mm thickness. The

magnets are enclosed in a heat-shrink tubing and fixed 1.1 mm apart by two laser-cut acrylic supports with their magnetic axes aligned with gravity and their like poles facing each other. This magnet module is inserted into alignment slots in the casing at a fixed distance from the camera module. Between the magnets and the camera, an aspheric lens (Adafruit, New York, NY) in a 3D-printed adjustable tube is placed such that the sample image is focused onto the camera. The lens extension tube is designed such that it screws into place and can be adjusted slightly via a user-accessible knob by turning the holder in the threads of the casing to achieve fine focusing capabilities when in use. Finally, a high-brightness, intensity-controlled white light LED (Adafruit, New York, NY) on a custom-printed circuit board (SeeedStudio, Shenzhen, China) are placed on the side of the magnets opposite the lens and camera in order to illuminate the sample with a user-defined light intensity. A light diffuser is also placed between the LED and the magnets in order to diffuse and collimate the light. A covering is fixed over the components, allowing manual access to the charging and USB ports, button presses, and a clear view of the TFT display screen, resulting in a compact, self-contained, and user friendly device.

Magnetic Levitation of Microspheres: Both size-controlled and density-controlled microspheres were used to characterize the function of the magnetic levitation platform. Size-controlled microspheres were obtained in three sizes: 5.35, 10.4, and 20 μm (Microspheres-Nanospheres, Cold Spring, NY). Density-controlled microspheres were obtained in 8 different densities: 0.96, 0.98, 0.995, 1.025, 1.050, 1.070, 1.090, 1.13 g cc^{-1} (Cospheric LLC, Santa Barbara, CA). Microspheres are mixed with a known concentration of paramagnetic medium, which is prepared by diluting Gadavist (Bayer, Whippany, NJ), which serves as a 1 M stock solution, in DI water (200×10^{-3} , 100×10^{-3} , 50×10^{-3} , 25×10^{-3} , and 12.5×10^{-3} M Gd). The sample, suspended in paramagnetic medium, is loaded into a square glass microcapillary tube with outer dimensions 1 mm by 1 mm and inner dimensions 0.7 mm by 0.7 mm via capillary action. The sample is then placed between the magnets through the opening in the casing. For time lapse images, images of the particles in the magnetic field were captured every 10 s, with time = 0 representing the time at which the sample was loaded into the device.

Image Processing: The pixel intensities are used to detect both the particles whose densities will be measured and the reference magnet and capillary edges. Pixel intensities are scanned in both Z- and Y-directions and the 1st order derivatives are calculated (where the Z-axis is parallel to the magnets and the Y-axis is parallel to the gravitational force). The average of the pixel intensities within Y-axis (vertical) slices over a Z-axis (horizontal) profile is calculated to obtain Y-derivatives. Likewise, Z-axis derivatives are obtained along Z-axis (horizontal) slices over a Y-axis (vertical) profile. Since the magnet and capillary edges lie along the Z-direction, they are filtered out in the Z-axis derivatives, which make it easier to detect the particles alone. Thus, the Z-derivative is used to calculate the average gradient at each height across a Y-profile and these means are plotted and fitted to a Gaussian curve to represent the distribution of the suspended particles. The software is capable of fitting multiple Gaussian curves to detect different particles, which can be triggered by the user.

The algorithm then outputs mean and variance values of the fitted curve for each image, describing the average levitation height of the particles and their degree of confinement, respectively. The inner edges of the magnets and the capillary are also automatically detected using the Y-derivative. The distance between the inner capillary edges, which is 0.7 mm, is used as a scale and the magnet edges are used for reference. The mean values are converted to millimeters using the obtained scale relative to the upper edge of the bottom magnet. The variance values are also converted to millimeters.

These values for variance from each respective image are fit to a time-lapse exponential decay curve. The time point on the curve at which the variance value is 20 μm is taken as the time to equilibrium; the value for mean measured from the corresponding time frame is taken as the equilibrium levitation height. These values are displayed in the graphical user interface.

WBC Cytometry: Whole blood was obtained via fingerstick in accordance with relevant University of Connecticut guidelines and regulations. All human experiments were approved by the University of Connecticut, protocol #H15-048. Informed consent was obtained from all subjects.

Whole blood was diluted (1:1000) in Gd (25×10^{-3} M) in HBSS. To observe an isolated population of WBCs at a higher concentration, whole blood was diluted 1:100 in ACK cell lysis buffer and incubated for 10 min before Gd was added (25×10^{-3} M final concentration). Samples were loaded into a capillary tube and levitated in the device for 10 min before imaging. Images were taken at various positions in the capillary to obtain a sampling of the cell population.

Supporting Information

Supporting Information is available from the Wiley Online Library or from the author.

Acknowledgements

B.Y. and S.K. contributed equally to this work. S.T. acknowledges the American Heart Association Scientist Development Grant (15SDG25080056) and the University of Connecticut Research Excellence Program award for financial support of this research. S.K. acknowledges that this material is based upon work supported by the National Science Foundation Graduate Research Fellowship (DGE-1247393). A provisional patent entitled "Magnetic Levitation with On-Board Optical Imaging and Image Analysis for Density-Based Separation, Identification, and Measurement" has been filed with UCONN Case No. 16-027 on the technology described here. S.T. and S.K. disclose a financial interest in a startup company, mBiotics, related to the technology described here.

Received: July 11, 2016

Revised: September 9, 2016

Published online: October 6, 2016

- [1] R. Pethig, *Biomicrofluidics* **2010**, *4*, 022811.
- [2] Y. Song, H. Yin, W. E. Huang, *Curr. Opin. Chem. Biol.* **2016**, *33*, 1.
- [3] D. Di Carlo, D. Irimia, R. G. Tompkins, M. Toner, *Proc. Natl. Acad. Sci. USA* **2007**, *104*, 18892.
- [4] C. W. Shields, C. D. Reyes, G. P. Lopez, *Lab Chip* **2015**, *15*, 1230.
- [5] S. Tasoglu, J. A. Khoory, H. C. Tekin, C. Thomas, A. E. Karnoub, I. C. Ghiran, U. Demirci, *Adv. Mater.* **2015**, *27*, 3901.
- [6] N. Pamme, *Lab Chip* **2006**, *6*, 24.
- [7] M. Hejazian, N.-T. Nguyen, *Biomicrofluidics* **2016**, *10*, 044103.
- [8] W. Zhao, R. Cheng, J. R. Miller, L. Mao, *Adv. Funct. Mater.* **2016**, *26*, 3916.
- [9] K. A. Mirica, F. Ilievski, A. K. Ellerbee, S. S. Shevkopyas, G. M. Whitesides, *Adv. Mater.* **2011**, *23*, 4134.
- [10] S. Tasoglu, C. H. Yu, H. I. Gungordu, S. Guven, T. Vural, U. Demirci, *Nat. Commun.* **2014**, *5*, 4702.
- [11] S. Tasoglu, D. Kavaz, U. A. Gurkan, S. Guven, P. Chen, R. Zheng, U. Demirci, *Adv. Mater.* **2013**, *25*, 1137.
- [12] A. B. Subramaniam, D. Yang, H.-D. Yu, A. Nemiroski, S. Tricard, A. K. Ellerbee, S. Soh, G. M. Whitesides, *Proc. Natl. Acad. Sci. USA* **2014**, *111*, 12980.
- [13] A. Winkleman, R. Perez-Castillejos, K. L. Gudiksen, S. T. Phillips, M. Prentiss, G. M. Whitesides, *Anal. Chem.* **2007**, *79*, 6542.
- [14] N. D. Shapiro, K. A. Mirica, S. Soh, S. T. Phillips, O. Taran, C. R. Mace, S. S. Shevkopyas, G. M. Whitesides, *J. Am. Chem. Soc.* **2012**, *134*, 5637.

- [15] N. D. Shapiro, S. Soh, K. A. Mirica, G. M. Whitesides, *Anal. Chem.* **2012**, *84*, 6166.
- [16] A. B. Subramaniam, M. Gonidec, N. D. Shapiro, K. M. Kresse, G. M. Whitesides, *Lab Chip* **2015**, *15*, 1009.
- [17] K. A. Mirica, S. T. Phillips, S. S. Shevkoplyas, G. M. Whitesides, *J. Am. Chem. Soc.* **2008**, *130*, 17678.
- [18] M. R. Lockett, K. A. Mirica, C. R. Mace, R. D. Blackledge, G. M. Whitesides, *J. Forensic Sci.* **2013**, *58*, 40.
- [19] M. B. J. Atkinson, D. K. Bwambok, J. Chen, P. D. Chopade, M. M. Thuo, C. R. Mace, K. A. Mirica, A. A. Kumar, A. S. Myerson, G. M. Whitesides, *Angew. Chem. Int. Ed.* **2013**, *52*, 10208.
- [20] S. Tasoglu, C. H. Yu, V. Liudanskaya, S. Guven, C. Migliaresi, U. Demirci, *Adv. Healthcare Mater.* **2015**, *4*, 1469.
- [21] K. A. Mirica, S. T. Phillips, C. R. Mace, G. M. Whitesides, *J. Agric. Food Chem.* **2010**, *58*, 6565.
- [22] A. Nemiroski, A. A. Kumar, S. Soh, D. V. Harburg, H. D. Yu, G. M. Whitesides, *Anal. Chem.* **2016**, *88*, 2666.
- [23] S. Knowlton, C. H. Yu, N. Jain, I. C. Ghiran, S. Tasoglu, *PLoS One* **2015**, *10*, e0134400.
- [24] R. Amin, S. Knowlton, B. Yenilmez, A. Hart, A. Joshi, S. Tasoglu, *RSC Adv.* **2016**, DOI: 10.1039/c6ra19483d.
- [25] S. M. Knowlton, I. Sencan, Y. Aytar, J. Khoory, M. M. Heeney, I. C. Ghiran, S. Tasoglu, *Sci. Rep.* **2015**, *5*, 15022.
- [26] B. Yenilmez, S. Knowlton, C. H. Yu, M. Heeney, S. Tasoglu, *Adv. Mater. Technol.* **2016**, *1*, 5, 1600100.
- [27] C. Briggs, I. Longair, P. Kumar, D. Singh, S. J. Machin, *J. Clin. Pathol.* **2012**, *65*, 1024.
- [28] *WHO compendium of innovative health technologies for low-resource settings: 2011-2014*, Point of Care Diagnostic Device for Total WBC, World Health Organization, Geneva, Switzerland, **2015**, pp. 111.
- [29] E. P. Furlani, *Permanent Magnet and Electromechanical Devices*, Academic Press, New York **2001**.
- [30] K. A. Mirica, S. S. Shevkoplyas, S. T. Phillips, M. Gupta, G. M. Whitesides, *J. Am. Chem. Soc.* **2009**, *131*, 10049.
- [31] Y. Takamura, K. Idegami, M. Kogi, H. Takabayashi, *Patent WO2012023298*, **2013**.
- [32] A. Ellerbee, S. Tricard, G. M. Whitesides, US Patent US20130314080 A1, **2012**.
- [33] S. Knowlton, C.H. Yu, F. Ersoy, S. Emadi, A. Khademhosseini, S. Tasoglu, *Biofabrication* **2016**, *8*, 25019.
- [34] R. Amin, S. Knowlton, A. Hart, B. Yenilmez, F. Ghaderinezhad, S. Katebifar, M. Messina, A. Khademhosseini, S. Tasoglu, *Biofabrication* **2016**, *8*, 22001.